Journal of Materials Chemistry A

Accepted Manuscript

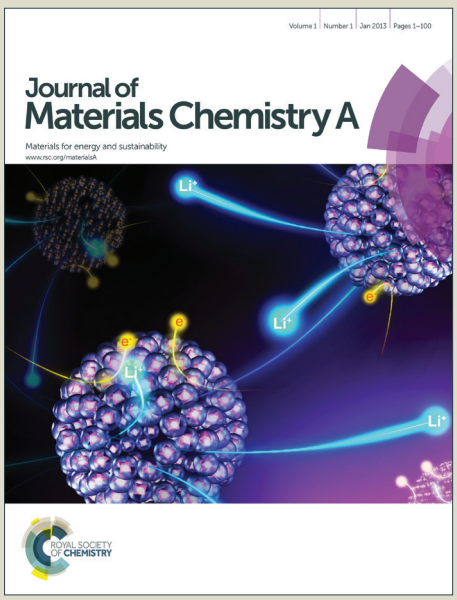

ROYAL SOCIETY OF CHEMISTRY

www.rsc.org/materialsA

Journal of

Materials Chemistry A

RSCPublishing

PAPER

Superlow load of nanosized MnO on the porous carbon matrix from wood fibre with superior lithium ion storage performance

Cite this: *J. Mater. Chem. A, x,* **x,** *x*

Received 00th January 2014,
Accepted 00th January 2014

DOI: 10.1039/x0xx00000x

www.rsc.org/

Chunxiao Yang,[a] Qiuming Gao,[a*] Weiqian Tian,[a] Yanli Tan,[a] Tao Zhang,[b] Kai Yang[a] and Lihua Zhu[a]

A facile synthesis of the MnO/C nanocomposite material consisting of 5.3 wt.% of MnO on the surface of porous carbon is introduced. Equally distributed nanosized MnO particles and the porous carbon matrix have fully developed synergetic effect to achieve superior lithium ion storage performance. Using the MnO/C nanocomposite material as the anode of Li-ion battery, a high discharge capacity of 952 mAh g^{-1} has been obtained at current density of 0.1 A g^{-1} with stable cycling performance over 100 charge/discharge cycles.

Introduction

Rechargeable lithium ion batteries (LIBs) have been intensively exploited[1-5] for portable electronic devices for the past decades and deemed as the most promising candidates to hybrid electric vehicles[6-8] and flexible portable electronic devices[9, 10]. Various transition metal oxides[11, 12] *e.g.*, SnO_2[13-16], TaC[17], CoO[18], MnO_x[19-23], etc. have been investigated to possibly substitute the unsatisfactory commercial graphite anode, among which MnO is one of the most potentials due to its relatively low electromotive force value (1.032 V vs. Li^+/Li), high theoretical capacity (756 mAh g^{-1}), high density (5.43 g cm^{-3}), low-cost, environmental benignity and natural abundance[24, 25]. However, the application of MnO to practical LIBs is still hampered by several challenges such as poor cycling stability caused by gradual aggregation of metal grains, structural pulverization due to large volume change during the repeated lithium ion insertion/extraction processes, and inferior rate capability as a result of low intrinsic conductivity[26]. An effective approach is to obtain the composite materials of MnO with a carbonaceous matrix, which acts as both a volume buffer and a conductive network to increase the electrical conductivity. To date, many kinds of carbonaceous matrixes for example graphenes[27-29], carbon nanotubes[22, 30, 31], polydopamines[32], polypyrroles[33], microalgaes[34], hemps[35, 36] and so forth have been used to fabricate the MnO/C composite anode materials. Among them, abundant and renewable biomass-derived carbons offered synthesis cost advantage over comparably performing designed nanocarbons, constructed amazing porous textures, and exhibited excellent electrochemical performances. For instance, Igor Kovalenko et al.[37] mixed Si nanopowder with alginate, a natural polysaccharide extracted from brown algae. Its capacity could retain 1200 mAh g^{-1} Si for more than 1300 cycles. Yi Cui group[38] used crab shell nanochannel templates to construct hollow nanofiber electrodes for rechargeable LIBs with specific capacity of 810 mAh g^{-1} after 200 cycles, which opened a new avenue for producing nanostructured electrode materials from low-cost sustainable sources. Sang Bok Lee team[39] utilized cellulose fibres with a porous internal structure as the substrate for the deposition of electrochemical energy storage materials to facilitate the ion diffusion process. David Mitlin group[36] created mesoporous three-dimensional (3D) MnO/CNS, consisting of a monolayer of MnO and hemp-derived carbon nanosheets. After 500 cycles of charge/discharge, the 3D MnO/CNS-2 (the MnO content = 73 wt.% and the BET specific surface area = 25 m^2 g^{-1}) composite could still keep a high reversible charge capacity of 900 mAh g^{-1}.

In this work, we assembled a novel kind of anode MnO/C nanocomposite material, consisting of superlow load of nanosized MnO grains on the surface of porous carbon from carbonized wood fibre. The wood fibres come from xylem of China fir (*Cunninghamia lanceolata (Lamb.) Hook.*) (referred to as "CF"), which is broadly cultivated in the south of China because it grows quickly without any special demands for climate, precipitation, or temperature. The CF xylem fibres are intrinsically soft, porous, and form into a multiple layered structure[40], mainly composing of cellulose, hemicellulose and lignin[41, 42]. After high temperature

carbonization, the tenuous carbonized fibres perfectly maintained the original morphology. Its 3D framework with multiple layers serves as a restrictive sheath to relieve the volume change and thus keeps the cell shape with strong tensile strength. Its porous structure possesses direct ionic pathways for better conductivity as the permits of the passage of nutrients such as water, ions and small molecules. The MnO/C nanocomposite material possessing of as high as 92 wt.% of carbon in the structure, shows an improved integral conductivity because the carbon has a much better conductivity than that of the MnO in the composite structure. Meanwhile, the nanosized MnO grains are evenly distributed on the surface of the porous carbon matrix, which leaves enough space for preventing the agglomeration during charge-discharge process. To our knowledge, our MnO/C nanocomposite material has the lowest content of MnO (5.3 wt.%), and the highest BET (Brunauer-Emmett-Teller) surface (429.1 $m^2 g^{-1}$) among the MnO/C composite materials. Consequently, evenly dispersed nanosized MnO particles on the porous carbon surface, provided a large fraction of Li^+ storage sites, emerging the Faradic redox pseudocapacitance action[43]. Carbonized fibres with abundant nanopores can give fully play to rapidly collect and release charge capacitance effect. Therefore, the MnO/C anode can achieve an excellent Li^+ storage performance by the strong synergistic effect between the MnO pseudocapacitance action and carbon capacitance effect[32, 44].

Experimental methods

Preparation of MnO/C

The CF was initially obtained from Henan province of China and air dried (water content < 20 wt.%). First, the CF xylem fibres were smashed and sieved to powder. Then, 1.00 g of the CF powder was washed three times in deionized water to remove the dissolved impurity. 0.05 g of $KMnO_4$ and 0.05 g of Na_2SO_4 were successively dissolved into 20 mL of deionized water with stirring until compete precursor solution for the soaking process. Subsequently, the CF powder was added into the above precursor solution and stirred for 1 h at room temperature. $KMnO_4$ reacted with the CF to form MnO_2[45]; Na_2SO_4 served as a buffer agent to keep the solution neutral. After soaked, the brown precipitates were filtered, washed and dried at 60°C for 12 h in an oven. In order to obtain the MnO/C composite material, the as-prepared precursor sample was placed inside an alumina boat in dimethylformamide (DMF) and heated in a tube furnace to 600°C at a rate of 2°C min^{-1} and kept for 4 h under a flowing N_2 atmosphere.

Cell assembly

The working electrodes were prepared by loading a slurry containing 70 wt.% active material (about 2.0 mg), 10 wt.% poly(vinylidenefluoride) (PVDF) [46] (in N-methylpyrrolidone) and 20 wt.% acetylene black on a nickel foam. After the electrode materials were loaded, the working electrode was pressed and dried in vacuum at 80°C for 12 h. The charge-discharge measurements were carried out using coin cells CR2032. A total of 2032 stainless steel coin sells with the MnO/C electrode and metal Li [47] by a porous polymeric separator were assembled with the electrolyte of 1 M $LiPF_6$ in a 1:1 (v/v) mixture of ethylene carbonate (EC) and dimethyl carbonate (DMC).

Characterization

The phase purity and crystalline structure of the sample were determined by using powder X-ray diffractometry (XRD, Labx XRD-6000, Shimadzu, Japan) with Cu Kα radiation (λ = 1.5418 Å) in the range of $10^o \leqslant 2\theta \leqslant 70^o$ (scan speed 3^o min^{-1} and scan step 0.02^o) at room temperature. Scanning electron microscopy (SEM) images of the carbons were observed on a Quanta-250 FEG (Holland) with 5 kV voltage and 10 μA current and a working distance 8~10 mm. (High resolution) transmission electron microscopy ((HR)TEM) observations were carried out at 200 kV on a JEOL JEM-2100F microscope with field-emission gun. X-ray photoelectron spectroscopy (XPS) analyses were conducted using Al Kα (150W) monochromatic X-ray source (ESCALAB 250, Thermo Fisher Scientific, USA). Thermogravimetric analyses (TGA) were examined at SDTQ600 (TA Instruments, USA) under air atmosphere at a heating rate of 10°C min^{-1} from room temperature to 800°C. Fourier transform infrared (FT-IR) spectra were performed on a Nicolet 6700 (Thermo Fisher Scientific, USA). Raman spectra were performed on a microscopic confocal Raman spectrometer (Lab RAM HR800) under a back scattering geometry (λ = 514 nm). N_2 sorption isotherms at 77 K were obtained on Micromeritics ASAP 2020. The sample was degassed at 300°C for 12 h. The electrochemical measurement experiments were carried out on a CHI660e electrochemical work station (Shanghai Chenhua Instruments Co., China) at room temperature. Electrochemical impedance spectroscopy (EIS) measurements were conducted for the working electrode in a frequency range of 0.01 Hz to 0.1 MHz. The EIS data were analysed using Nyquist plots, which represent the real part (Z') and imaginary part (Z'') of impedance.

Results and discussion

The facile fabrication process of MnO/C is illustrated in Figure 1a. Natural wood has a 3D porous structure with multiple layers. The xylem of CF is composed of slight fibres. The CF xylem fibres blended with $KMnO_4$ in the neutral Na_2SO_4 solution to form the MnO_2/CF precursor[48]. The as-prepared precursor in the DMF solution was calcined[49] in N_2 to obtain the MnO/C composite material. From the SEM images (Fig. 1b), it clearly shows that the natural wood fibre without any chemical treatment has a curving multilayered sheet structure. After soaked with $KMnO_4$ in the Na_2SO_4 solution, the CF fibre surface with undamaged appearance (Fig. 1c) was inlayed with the MnO_2. TEM images (Fig. S1) exhibited the relatively gathered distribution of MnO_2. After the carbonization (Fig. 1 d and e), it clearly depicts that the carbonated CF perfectly maintained the original fibres' morphology, which has multilayered walls and 3D tortuous structure. HRTEM examination exhibits the detailed microstructure of the MnO/C sample. Figure 1f shows the well-crystallized MnO nanoparticles[45] with diameters ranging from 3 to 7 nm are evenly dispersed on the carbon matrix (also see Fig. S2)[50]. Further enlarged HRTEM image of the MnO/C sample (Fig. 1g) clearly demonstrates the periodic lattice fringes with distinct interplanar distance of 0.26 and 0.22 nm corresponding

to the (111) and (200) plane of cubic MnO, respectively[51]. Thus, a unique nanoarchitecture of the carbon-supported MnO can be readily identified.

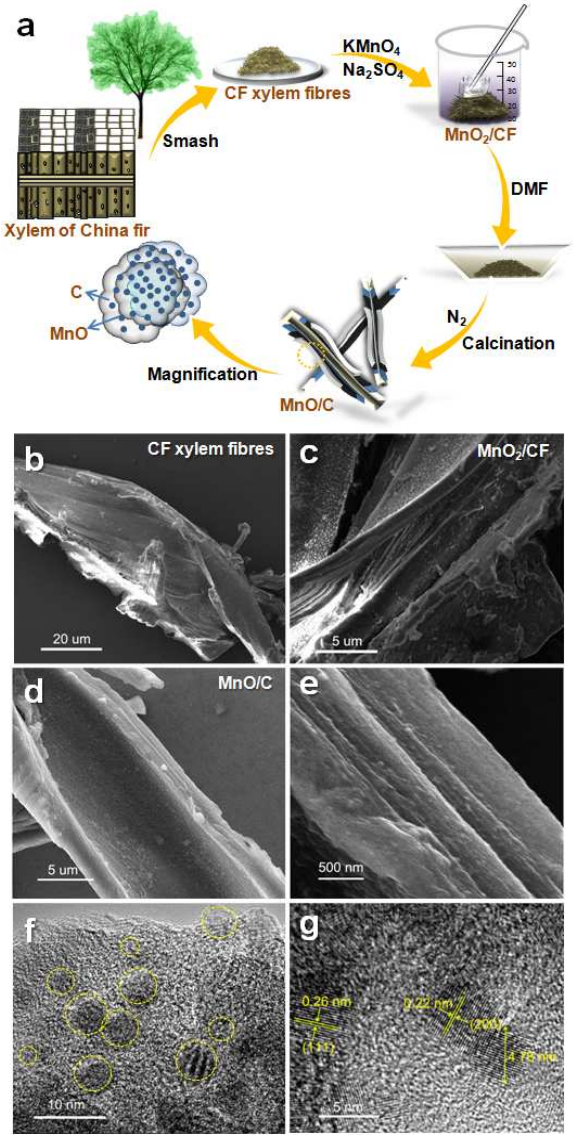

Fig. 1 (a) The fabrication scheme of MnO/C sample, (b and c) SEM images of the MnO/C sample, and (d-g) the (HR)TEM images of the MnO/C sample. The well-crystallized MnO nanoparticles with diameters ranging from 3 to 7 nm are evenly dispersed on the carbon matrix. The periodic lattice fringe with distinct interplanar distance of 0.26 and 0.22 nm is corresponding to the (111) and (200) plane of cubic MnO, respectively (g).

XRD patterns of the natural CF, MnO_2/CF precursor and MnO/C samples are shown in Figure 2a. The major wood component, cellulose, is stabilized by the hydrogen bonds and van der Waals forces between the hydroxyl groups on the D-glucose units, resulting in some crystalline character in the natural CF. The XRD patterns of the natural CF show a wide diffraction peak at 22.83° and a small peak at 15.02° due to the (101) and (002) crystal plane of cellulose, respectively. The natural CF's multiple layers could be also observed from the TEM images (Fig. S3 a and b). A small XRD peak at 34.14° appeared when the hydroxyl in cellulose reacted with $KMnO_4$ in the neutral Na_2SO_4 solution. This peak is corresponding to the characteristic (100) crystal plane of MnO_2 (JCPDS No. 42-1169). The HRTEM (Fig. S1b) images indicated that the MnO_2 with interplanar distance of 0.24 nm is anchored on the carbon matrix[52], which is in coincidence with the XRD results. Two typical bands at 642.1 and 653.9 eV corresponding to the $2p_{3/2}$ and $2p_{1/2}$ orbits of Mn^{4+} were observed in the XPS of MnO_2/CF (Fig. S4a) further proved the existence of MnO_2 on the MnO_2/CF composite surface. The $KMnO_4$ could react at the chain end on the surface of the crystallites, resulting in a slightly decreased intensity of the cellulose characteristic peaks. In this case, the intensity of the cellulose characteristic peak at 22.83° increased a little, thus the oxidation reaction mainly took place in the amorphous region of CF cellulose because of the difficulty of destruction of the polymer chains in the crystalline regions of cellulose[53]. The XRD peaks at 35.18°, 40.82° and 58.96° due to the (111), (200) and (220) crystal planes of MnO (JCPDS No. 07-0230) were observed for the MnO/C composite, which are in consistent with the HRTEM images observation in Figure 1g. XPS of the MnO/C sample were given in Figure S4b to confirm the existence of MnO on the MnO/C composite surface. The two signals at 641.5 and 653.3 eV may be attributed to the Mn (II) $2p_{3/2}$ and $2p_{1/2}$ orbits, respectively, characteristic of MnO [33]. The XPS of O 1s orbit is shown in Figure S4c. The band at 532.4, 531.5 and 530.0 eV can be assigned to the oxygen bond of C-OH phenol groups and/or C-O-C ether groups[54], Mn-O and C=O, respectively[50]. There is a strong C 1s peak at 284.9 eV in Figure S4d, corresponding to the graphitic carbon. The weaker one at 286.1 eV arising from the C-O, while the peak at about 288.5 eV indicates the formation of C=O bonds[50].

FT-IR spectra of the natural CF, MnO_2/CF and MnO/C samples are shown in Figure 2b. All samples exhibited the same characteristic absorption band at 3130 cm^{-1} assignable to the vibrations of hydroxyl groups[53]. When the cellulose reduced $KMnO_4$ to MnO_2[20, 23], more hydroxyls formed, resulting in an obviously broader ν_{O-H} band of the MnO_2/CF precursor than that of the natural CF's. The associated hydroxyls were destroyed during the heating process, leading to a narrower ν_{O-H} band of the MnO/C sample. The observed bands at 1600 cm^{-1} may be attributed to the C=C stretching vibrations, deducing the existence of furanic and aromatic groups[55, 56]. The band at 1402 and 1134 cm^{-1} can be ascribed to the carboxylic O-H deformation vibration and the C-O-C stretching vibration, respectively[57].

TGA curves of the obtained MnO/C sample (Fig. 2c) were used to examine the MnO content in the nanocomposite material. About 2.58 wt.% of weight loss occurred before 150°C due to the loss of water. Zaki et al. reported that MnO has transformed to Mn_2O_3 after a heat treatment between 500 and 1050°C in the oxygen atmosphere[58]. Therefore, it is reasonable to believe that the slight weight increase of 1.06 wt.% in the TGA curve starting from 150 up to 280°C corresponds to the joint results of the oxidation of MnO into Mn_2O_3 and the loss of residual H_2O. Subsequently, there is a huge weight loss process (86.51 wt.%) from 280 to 420°C, which can be mainly attributed to the combustion of carbon to CO_2 and partial oxidation of MnO into Mn_2O_3. When the temperature reaches 800°C, the carbon is completely combusted. Meanwhile, the MnO

totally transforms to Mn_2O_3, which has been caused about 11.28 wt.% weight gain. Therefore, the weight percentage of MnO in the composite sample is 5.3 wt.%. The low amounts of Mn element in the MnO/C nanocomposite resulted in the weak intensities of the XRD peaks in Figure 2a.

The MnO/C nanocomposite material was further analyzed by Raman spectroscopy (Fig. 2d). There are two bands at 1344 and 1603 cm^{-1}, which is related to the A_{1g} vibration mode of the disordered carbon (D-bond) and the E_{2g} vibration mode of the ordered graphitic carbon (G-bond), respectively. The I_D/I_G value (ratio of the intensities of D-band and G-band) of the MnO/C nanocomposite material is 0.9, which is much higher than that of the fully graphitized carbon, revealing a relatively high defective state of the carbon matrix. This defective structure may be favourable to enhance the ionic conductivity of electrolyte. Besides, a distinct band at 654 cm^{-1} belonging to Mn_3O_4 rather than MnO was observed for the MnO/C nanocomposite material. The MnO is easily transformed into Mn_3O_4, caused by the local heating effect and photochemically induced transformations when the beam intensity is more than 1.1 MW during the Raman measurements[31].

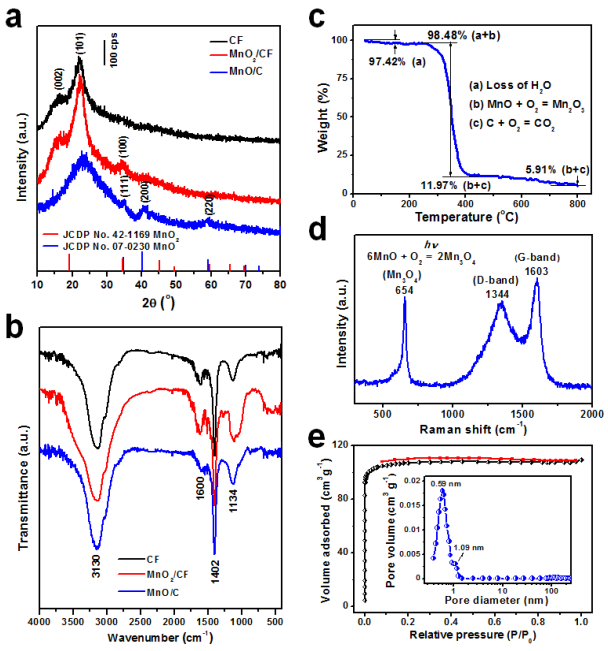

Fig. 2 (a) XRD patterns and (b) FTIR spectra of the CF, MnO_2/CF and MnO/C samples. And (c) TGA curve, (d) Raman spectrum and (e) N_2 sorption isotherms of the MnO/C nanocomposite material. The insert of (e) is the pore size distribution curve calculated from the adsorption branch by the density functional theory (DFT) model.

N_2 sorption isotherms for the MnO/C nanocomposite material are showed in Figure 2e with the insert of its pore size distribution. The adsorption curve of the MnO/C sample shows a typical I-isotherm with a little hysteresis between the adsorption and desorption branches, which is characteristic for the microporous material (S_{mi}/S_t = 78.4%) with some mesopores. The BET specific surface area of the MnO/C sample is measured to be about 429.1 m^2 g^{-1}. High microporosity and large specific surface may be contributed greatly to the development of carbon's capacitance effect[59]. The main pore size distribution is at 0.59 nm, which is much smaller than that of the MnO grain (3-7 nm) based on the HRTEM image (Fig. 1c) observation. Thus, we can speculate that the nanosized MnO grains cannot permeate into the pores of carbon, *i.e.*, the MnO grains exist on the surface of the carbon. The N_2 sorption isotherms for the pure carbon (from CF) are showed in Figure S5 with the insert of its pore size distribution. The BET specific surface area of the pure carbon sample is about 501.9 m^2 g^{-1}. Since the MnO grains may decrease the specific surface areas to some extent due to the increased effective mass of the composite, the small amount of loss (72.8 m^2 g^{-1}) could be observed on the specific surface area of the MnO/C composite (429.1 m^2 g^{-1}). Meanwhile, the main pore size distribution is at 0.54 nm for the pure carbon sample, which is close to that of the MnO/C sample (0.59 nm). So, it is confirmed that the nanosized MnO grains mainly evenly anchored on the surface of the porous carbon matrix without blocking the microspores of the carbon.

When serving as an anode material for the LIBs, the MnO/C nanocomposite material revealed a superior Li^+ storage performance. All tested specific capacities were calculated on the mass of the whole composite sample, *i.e.*, the mass sum of MnO plus C. The cyclic voltammetry (CV) curves of the electrode containing the MnO/C nanocomposite material for the first four cycles in the voltage range 0.01-3.0 V versus Li/Li^+ at a scan rate of 0.1 mV s^{-1} are shown in Figure 3a. As to the cathodic sweep from 3.0 to 0.01 V, one small peak could be observed at 1.4 V and disappeared in the subsequent cycles. It may be ascribed to the reduction of Mn^{3+} or Mn^{4+} to Mn^{2+}, which was derived from the incomplete reduction of MnO_2 in the calcination process[21, 24]. There was a poignant reduction peak near to 0.5 V in the first cathodic sweep, which corresponds to the reduction of Mn^{2+} to metal Mn (MnO + $2Li^+$ + 2e ⇔ Mn + Li_2O)[60]. In the case of the anodic sweep from 0.01 to 3.0 V, the electrode showed a slope related to the oxidation of Mn^0 to Mn^{2+} in the voltage range between 1.0 and 1.5 V. The curves of the MnO/C nanocomposite material tested at higher scan rates of 1 mV s^{-1} (Fig. S6) displayed both quasi-rectangular shape and redox peaks, which indicate that the nanosized MnO and porous carbon cooperatively get an excellent Li^+ storage performance in the MnO/C nanocomposite material[29].

Figure 3b presents the potential versus capacity traces of the electrode containing the MnO/C nanocomposite material at the current density of 0.1 A g^{-1}. In the first discharge process, a well-defined conversion plateau at 0.1 V (vs. Li^+/Li) was observed, corresponding to the reduction of Mn^{2+} to Mn^0. The initial discharge and charge capacity of the MnO/C nanocomposite material was obtained at 1620 and 888 mAh g^{-1}, respectively, accounting for an initial Coulombic efficiency of 54.8%, which may be mainly attributed to the irreversible processes such as inevitable formation of a solid electrolyte interface (SEI) layer and a certain extent electrolyte decomposition. From the second cycle on, the discharge capacity gradually became lower, presenting a common capacity fading. It is interesting to see that the capacity starts to increase after 35 cycles (Fig. 3c), which was also observed in other reported

nanostructured Mn-based oxides[21, 61]. After 100 cycles of charge/discharge treatments, the MnO/C nanocomposite material could still keep a high reversible charge capacity of 952 mAh g^{-1}, showing its excellent cycle stability. The Coulombic efficiency steadily reached around 99% accompanied by the cycle number increasing. In this case, the initial discharge capacity of the pure carbon material (Fig S7) was 426 mAh g^{-1}, which is a little higher than the theoretical capacity of carbon (372 mAh g^{-1}). After 10 cycles, the pure carbon material could still keep a reversible charge capacity of 386 mAh g^{-1}. The carbon with stable 3D porous structure serves as a restrictive sheath to relieve the volume change, benefiting for the cycle stability of MnO/C nanocomposite material.

The rate capability and cycle stability of the MnO/C nanocomposite material were further examined and are illustrated in Figure 3d. The cell was first tested at the current density of 0.1 A g^{-1}, and then the charge-discharge current density was successively increased to 0.2, 0.5, 1 and 3 A g^{-1}. The corresponding average charge capacity for 10 cycles was measured as 780, 674, 571, 386 and 275 mAh g^{-1}, respectively. When the current density was decreased back to 0.1 A g^{-1}, an average capacity of 604.0 mAh g^{-1} was recovered, indicating its excellent rate capability and cycle stability.

It should be clarified that the MnO/C nanocomposite materials with different calcination temperatures (Fig. S8 a and b) and MnO contents (Fig. S9) were well tested to get the optimum experimental condition (Fig. S10). TGA (Fig. S11) were used to examine the MnO contents in the nanocomposite materials. The HRTEM images (Fig S12) of the MnO/C electrodes with different MnO contents indicate that there are some high dispersion MnO particles with the particle sizes of about 2-5 nm for MnO/C-1.9 containing 1.9 wt.% of MnO. As to the MnO/C-8.9 with 8.9 wt.% of MnO, there are more MnO particles with the larger particle sizes of about 5-10 nm on the surface of the carbons and some MnO particles aggregated together. The big MnO particles and aggregates may result in the reduction of contact area between the MnO and carbon, against the development of synergistic effect. Besides, the MnO is much heavier than carbon, which will increase the mass of active material, resulting in a decreased specific capacity. The MnO contents, BET specific surface areas, first discharge specific capacities and specific capacities after cycles of the MnO/C composite materials obtained by different methods[22, 25, 28, 31, 33, 34, 36, 62, 63] were summarized in Figure 3e (the details were shown in Table S1). Apparently, the MnO/C composite material from our work has the lowest MnO content (5.3 wt.%) and the highest BET surface (429.1 m^2 g^{-1}) among all the MnO/C composite materials. Before carbonization the MnO_2 has already anchored on the surface of CF, following with the reaction that the MnO_2 was reduced to MnO during the calcination. Slight reduce of BET specific surface areas and almost unchanged main pore size distribution from the pure carbon to MnO/C composites material confirm that the MnO mainly exist on the surface of carbon and does not block the newly forming pores. The spherical MnO which equally distributed on the surface synergetic cooperates with the porous carbon resulting in the enhanced Li^+ storage performance.

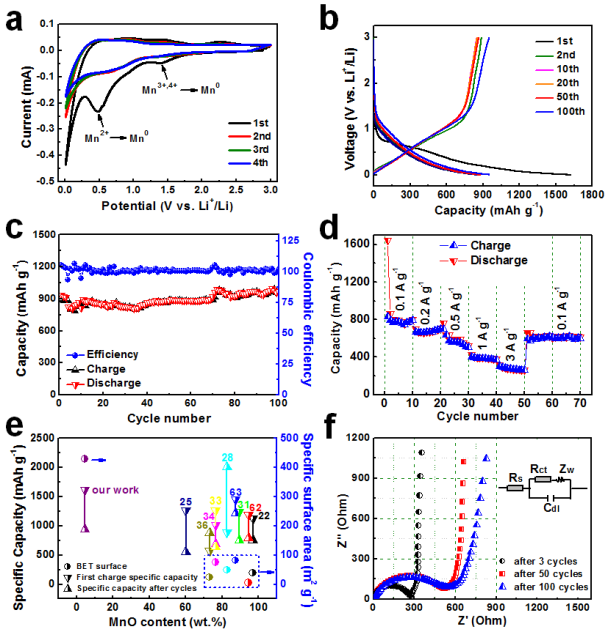

Fig. 3 (a) CV curves at a scan rate of 0.1 mV s^{-1}. (b) Charge-discharge profiles of the electrode containing MnO/C sample for cycles with a current density of 0.1 A g^{-1}. (c) Cycling performance and Columbic efficiency at a current density of 0.1 A g^{-1}. (d) Rate performance of the electrode containing the MnO/C sample. (e) Summarized the MnO content, BET specific surface area, first discharge specific capacity and specific capacity after cycles of the MnO/C composite samples by different methods with the related reference number. And (f) the Nyquist plots of the electrode containing the MnO/C sample after 3, 50 and 100 cycles, where the insert is the simulation model of the equivalent circuit.

EIS of the electrodes containing the MnO/C nanocomposite material after 3, 50 and 100 cycles were determined and the Nyquist plots are given in Figure 3f. The EIS can be explained on the basis of an equivalent circuit model[29], as an insert indicated in Figure 3f. There are three distinct parts in the Nyquist plots: one is the intercept of the high-frequency semicircle on the real axis can be attributed to the resistance of electrolyte (R_s). The middle frequency semicircle is associated with the charge transfer resistance (R_{ct}) and the double layer capacitance. The slope line at low frequency is related to the Warburg impedance (Z_w) of the lithium-ion diffusion. The curves are more vertical to the real axis, the cell is more close to an ideal capacitor[64]. The R_s for the MnO/C system after 100 cycles is 5.2 Ω. This value is higher than that with 50 cycles (3.9 Ω) and 3 cycles (2.4 Ω). These values mean that the resistances of the electrolyte systems are all small and increased by cycles. The R_{ct} of the electrode containing the MnO/C material increased from about 271 Ω after 3 cycles to 522 Ω after 50 cycles possibly due to the continuously densified SEI layer of the electrode hampers the electron transmission. After 100 cycles the R_{ct} gradually increased slightly to 551 Ω compared to that after 50 cycles (522 Ω), which demonstrates that the densified SEI layer structure is stabilized and hardly changed in the later 50 cycles. The slope in low-frequency region was almost vertical to the real axis due to the rich pore textures, which benefit for the ionic transportation of the electrolyte onto the surface of the electrode in the system. The diffusion coefficient (D) values of the lithium ions can be obtained from the equation[65]: $D = 0.5(R \cdot T/(A \cdot F^2 \cdot \sigma_w \cdot C)^2$, where σ_w is the slope for the

plot of Z′ vs. the reciprocal root square of the low angular frequencies ($\omega^{-1/2}$). The plot of Z′ vs. $\omega^{-1/2}$ for MnO/C after 3 cycles is shown in Figure S13. The D value of MnO/C electrode after 3, 50 and 100 cycles is 2.2×10^{-12}, 1.8×10^{-12} and 1.0×10^{-12} cm^2 s^{-1}, respectively. The diffusion coefficients decreased a little due to a certain extent aggregation of the nanosized MnO grains[66] on the porous carbon matrix in the later cycles. The Nyquist plots of the MnO/C electrode with various MnO contents were further tested and shown in Figure S14, and their related parameter were illuatrated in Table S2. The MnO/C possesses the largest D value among the composite samples with different MnO contents (Table S2). Therefore, the abundant pore textures in the MnO/C composite material can sufficiently develop the charge capacitance effect of carbon without sacrificing the pseudocapacitance of MnO, which is quite benefit for the maintenance of the high discharge capacity, large rate capability and long-time cycle stability.

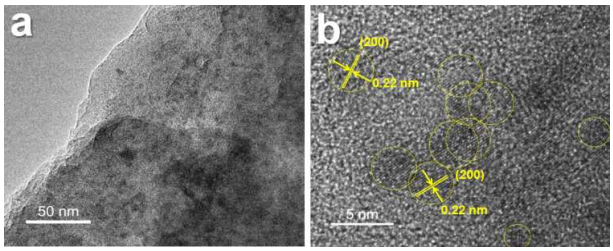

Fig. 4 TEM (a) and HRTEM (b) images of the MnO/C sample charged to 3 V after 100 cycles at the current density of 0.1 A g^{-1}. The size of MnO grains is about 2-5 nm due to a hundred times redox reaction (a and b). The fringe spacing values of the domains are about 0.22 nm, corresponding to the (200) plane of the MnO (b).

The convictive evidence of the structural stability of the MnO/C electrode material was further revealed by the (HR)TEM images of the MnO sample after 100 times cycles. The MnO grains still exhibited homogeneous distribution (Fig. 4a) on the surface of the porous carbon matrix. Their original spherical morphology was mainly maintained with slightly partial agglomeration and deformation based on the HRTEM images of the MnO/C sample shown in Figure 4b. Simultaneously, the size of MnO grains decreased a little to 2-5 nm (Fig. 4b) due to a hundred times redox reaction. The fringe spacing values of these domains are about 0.22 nm, corresponding to the (200) plane of the MnO. No pulverization could be found in the MnO/C electrode material, indicating that the porous carbon structure can effectively remit the strain and stress of volume change during the charge/discharge processes, which consequently heightens the cycle stability and rate capability.

Conclusions

We have demonstrated the facile synthesis of superior lithium ion storage performance MnO/C nanocomposite anode material consisting of superlow load of MnO and porous carbon matrix. This unique structure and strong synergistic effect between the nanosized MnO particles and porous carbon matrixes lead to a high discharge capacity, a stable cycle stability and an excellent rate performance. Insight gained from this work, the content of MnO doesn't directly proportional to electrochemical properties. Low content and evenly distributed nanosized MnO may be more conducive to better lithium storage performance. In addition, our unique nanocomposite structure provides considerable freedom in structural variability considering the vast options of transition metal oxide and carbon-based material, which can be extended to other promising high performance anode materials for the future development of novel energy storage materials.

Acknowledgement

This work was supported by National Basic Research Programs of China (973 Programs, No. 2011CB935700 and 2014CB931800), Chinese Aeronautic Project (No. 2013ZF51069) and Chinese National Science Foundation (No. U0734002).

Notes and references

[a]Key Laboratory of Bio-inspired Smart Interfacial Science and Technology of Ministry of Education, Beijing Key Laboratory of Bio-inspired Energy Materials and Devices, School of Chemistry and Environment, Beihang University, Beijing 100191, P. R. China. [b]Beijing Centre for Physical and Chemical Analysis, Beijing 100089, P. R. China. Correspondence should be addressed to Q. Gao. E-mail: qmgao@buaa.edu.cn.Tel: +861082338212. Fax: +861082338212.

Electronic Supplementary Information (ESI) available: Preparation of the MnO/C with different contents of MnO, (HR)TEM images of the MnO_2/CF, MnO/C and natural CF with different enlargements, XPS spectra of the MnO_2/CF and MnO/C, N_2 sorption isotherms and pore size distribution of the pure carbon, electrochemistry capacity of the pure carbon, electrochemical measurement of the MnO/C electrodes with different calcination temperature and different MnO contents, TGA curves and the HRTEM images of the MnO/C electrodes with different MnO contents, the Nyquist plots of the MnO/C electrodes with various MnO contents and their related parameters, the relationship between Z′ and $\omega^{-1/2}$ at low frequency for the MnO/C, the comparison of the MnO content, BET specific surface area and specific capacity of the MnO/C composite materials by different methods, as well as comparison of the resistance of electrolyte (R_s), the charge transfer resistance (R_{ct}) and diffusion coefficient (D) of the MnO/C composite sample with various MnO contents. See DOI: 10.1039/c000000x/

1. Y. Xia, W. Zhang, Z. Xiao, H. Huang, H. Zeng, X. Chen, F. Chen, Y. Gan and X. Tao, *J. Mater. Chem.*, 2012, **22**, 9209-9215.
2. B. Jang, M. Park, O. B. Chae, S. Park, Y. Kim, S. M. Oh, Y. Piao and T. Hyeon, *J. Am. Chem. Soc.*, 2012, **134**, 15010-15015.
3. K. Kang, K. Song, K. Heo, S. Yoo, G.-S. Kim. G. Y-M Kang and M-H. Jo, *Chem. Sci.*, 2011, **2**, 1090-1093.
4. Y. Liang, P. Zhang and J. Chen, *Chem. Sci.*, 2013, **4**, 1330-1337.
5. L. Wang, D. Wang, Z. Dong, F. Zhang and J. Jin, *Small*, 2014, **10**, 998-1007.
6. G. Jeong, Y.-U. Kim, H. Kim, Y.-J. Kim and H.-J. Sohn, *Energy Environ. Sci.*, 2011, **4**, 1986-2002.
7. A. E. Ismanto, S. Wang, F. E. Soetaredjo and S. Ismadji, *Biores. Tech.*, 2010, **101**, 3534-3540.
8. J. M. Tarascon, M. Armand, *Nature*, 2001, **414**, 359-367.
9. Y. Hu and X. Sun, *J. Mater. Chem.*, 2014, **2**, 10712-10738.

10. C. Yan and P. S. Lee, *Small*, 2014, **10**, 2-15.
11. H. Kim, G. Jeong, Y. U. Kim, J. H. Kim, C. M. Park and H. J. Sohn, *Chem. Soc. Rev.*, 2013, **42**, 9011-9034.
12. W.-W. Lee and J.-M. Lee, *J. Mater. Chem. A*, 2014, **2**, 1589-1626.
13. X. Zhou, L. Wan and Y. Guo, *Adv. Mater.*, 2013, **25**, 2152-2157.
14. L. Wang, D. Wang, Z. Dong, F. Zhang and J. Jin, *Nano Lett.*, 2013, **13**, 1711-1716.
15. J. Lin, Z. Peng, C. Xiang, G. Ruan, Z. Yan, D. Natelson and J. M. Tour, *ACS Nano*, 2013, **7**, 6001-6006.
16. W.-H. Qu, F. Han, A.-H. Lu, C. Xing and W.-C. Li, *J. Mater. Chem. A*, 2014, **2**, 6549-6557.
17. X. Tao, J. Du, Y. Li, Y. Yang,Yang, Z. Fan, Y. Gan, H. Huang, W. Zhang, L. Dong and X. Li, *Adv. Ener. Mater.*, 2011, **1**, 534-539.
18. B. C. Cheng, X. Peng, Y. Qin, S. Yang, C. Li, S. Liu and J. Yang, *ACS Nano*, 2012, **6**, 1074-1081
19. I. Nam, N. D. Kim, G.-P. Kim, J. Park and J. Yi, *J. Power Sources*, 2013, **244**, 56-62.
20. G. Zhao, J. Li, L. Jiang, H. Dong, X. Wang and W. Hu, *Chem. Sci.*, 2012, **3**, 433-437.
21. J. Guo, Q. Liu, C. Wang, Q. Wang and M. R. Zachariah, *Adv. Funct. Mater.*, 2012, **22**, 803-811.
22. G. Xu, Y. Xu, H. Sun, F. Fu, X. Zheng, L. Huang, J. Li, S. Yang and S. Sun, *Chem. Commun.*, 2012, **48**, 8502-8504.
23. J. Zang and X. Li, *J. Mater. Chem.*, 2011, **21**, 10965-10969.
24. B. Sun, Z. Chen, H.-S. Kim, H. Ahn and G. Wang, *J. Power Sources*, 2011, **196**, 3346-3349.
25. X. Zhang, Z. Xing, L. Wang, Y. Zhu, Q. Li, J. Liang, Y. Yu, T. Huang, K. Tang, Y. Qian and X. Shen, *J. Mater. Chem.*, 2012, **22**, 17864-17869.
26. V. Etacheri, R. Marom, R. Elazari, G. Salitra and D. Aurbach, *Energy Environ. Sci.*, 2011, **4**, 3243-3262.
27. K. H. Zhang, P. Gu, L. Zhang, L. Liu, Z. Kong, Q. Zhang, C. Dong, S. Zhang, Z. Yao, J. Xu, H. Cui, G. Cui and L. Chen, *ACS Appl. Mater. Interf.*, 2012, **4**, 658-664.
28. Y. Sun, X. Hu, W. Luo, F. Xia and Y. Huang, *Adv. Funct. Mater.*, 2013, **23**, 2436-2444.
29. Q. Liao, N. Li, H. Cui and C. Wang, *J. Mater. Chem.*, 2013, **1**, 13715-13720.
30. Y. Ding, C. Wu, H. Yu, J. Xie, G. Cao, T. Zhu, X. Zhao and Y. Zeng, *Electrochim. Acta*, 2011, **56**, 5844-5848.
31. X. Li, Y. Zhu, X. Zhang, J. Liang and Y. Qian, *RSC Adv.*, 2013, **3**, 10001-10006.
32. H. Jiang, Y. Hu,S. Guo, C. Yan, P. S. Lee and C. Li, *ACS Nano*, 2014, **6**, 6038-6046.
33. W. Chen, L. Qie, Y. Shen, Y. Sun, L. Yuan, X. Hu, W. Zhang and Y. Huang, *Nano Energy*, 2013, **2**, 412-418.
34. Y. Xia, X. Dou, H. Huang, X. Lu, R. Yan, Y. Gan, W. Zhu, J. Tu, W. Zhang and X. Tao, *ACS Nano*, 2013, **7**, 7083-7092.
35. H. Wang, A. Kohandehghan, Z. Li, K. Cui, X. Tan, and D. Mitlin, *ACS Nano*, 2013, **7**, 5131-5141.
36. H. Wang, Z. Xu, Z. Li, K. Cui, J. Ding, A. Kohandehghan, X. Tan, B. Zahiri, B. C. Olsen, C. M. Holt and D. Mitlin, *Nano Lett.*, 2014, **14**, 1987-1994.
37. I. Kovalenko, B. Zdyrko, A. Magasinski, B. Hertzberg, Z. Milicev, R. Burtovyy, I. Luzinov and G. Yushin, *Science*, 2011, **334**, 75-79.
38. H. Yao, G. Zheng, W. Li, M. T. McDowell, Z. Seh, N. Liu, Z. Lu and Y. Cui, *Nano Lett.*, 2013, **13**, 3385-3390.
39. Z. Gui, E. Gillette, X. Han, G. W. Rubloff, L. Hu and S. B. Lee, *ACS Nano*, 2013, **7**, 6037-6046.
40. M. Bourourou, K. Elouarzaki, M. Holzinger, C. Agnès, A. L. Goff, N. Reverdy-Bruas, D. Chaussy, M. Party, A. Maaref and S. Cosnier, *Chem. Sci.*, 2014, **5**, 2885-2888.
41. M. Fan, D. Dai and A. Yang, *Int. J. Polymer. Mater.*, 2011, **60**, 1026-1040.
42. H. Zhu, Z. Jia, Y. Chen, N. Weadock, J. Wan, O. Vaaland, X. Han, T. Li and L. Hu, *Nano Lett.*, 2013, **13**, 3093-3100.
43. P. Simon, Y. Gogotsi and B. Dunn, *Science*, 2014, **343**, 1210-1211.
44. H. Jiang, J. Ma and C. Li, *Adv. Mater.*, 2012, **24**, 4197-4202.
45. C. K. Remucal and M. Ginder-Vogel, Environ. *Sci. Process Impacts*, 2014, **16**, 1247-1266.
46. Z. W. Seh, Q. Zhang, W. Li, G. Zheng, H. Yao and Y. Cui, *Chem. Sci.*, 2013, **4**, 3673-3677.
47. A. S. Gietter, R. C. Pupillo, Glenn P. A. Yap, T. P. Beebe, Jr., J. Rosenthal and D. A. Watson, *Chem. Sci.*, 2013, **4**, 437-443.
48. C. K. Remucal and M. Ginder-Vogel, *Environ. Sci. Process Impacts*, 2014, **16**, 1247-1266.
49. G. Xu, Y. Xu, J. Fang, F. Fu, H. Sun, L. Huang, S. Yang and S. Sun, *ACS Appl. Mater. Interf.*, 2013, **5**, 6316-6323.
50. M. Yang, Y. Zhong, X Zhou, J. Ren, L. Su, J. Wei and Z. Zhou, *J. Mater. Chem. A*, 2014, **2**, 12519-12525.
51. K. Su, C. Wang, H. Nie, Y. Guan, F. Liu and J. Chen, *J. Mater. Chem. A*, 2014, **2**, 10000-10006.
52. D. Su, H.-J. Ahn and G. Wang. *J. Mater. Chem. A*, 2013, **1**, 4845-4850.
53. D. Kim, Y. Andou, Y. Shirai, and H. Nishida, *ACS Appl. Mater. Interf.*, 2011, **3**, 385-391.
54. D. Hulicova-Jurcakova, M. Seredych, G. Lu and T. J. Bandosz. *Adv. Funct. Mater.*, 2009, **19**, 438-447.
55. B. Grzyb, C. Hildenbrand, S. D. Bégin, N. Job, A. Rigacci and P. Achard, *Carbon*, 2010, **48**, 2297-2307.
56. X. Sun and Y. Li, *Angew. Chem. Int. Ed.*, 2004, **43**, 597-601.
57. C. Moreno-Castilla, M. V. Lopze-Roman and F. Carrasco-Marin, *Carbon*, 2000, **38**, 1995-2001.
58. M. I. Zaki, M. A. Hasan, L. Pasupulety and K. Kumari, *Thermochim. Acta*, 1997, **303**, 171-181.
59. J. Xu, Q. Gao, Y. Zhang, Y. Tan, W. Tian, L. Zhu and L. Jiang, *Sci. Rep.*, 2014, **4**, 5545.
60. X. Ma, Q. Wan, X. Huang, C. Ding, Y. Jin, Y. Guan and C. Chen, *Electrochim. Acta*, 2014, **121**, 15-20.
61. F. M. Courtel, H. Duncan, Y. Abu-Lebdeh and I. J. Davidson, *J. Mater. Chem.*, 2011, **21**, 10206-10218.
62. X. Li, S. Xiong, J. Li, X. Liang, J. Wang, J. Bai and Y. Qian, *Chemistry*, 2013, **19**, 11310-11319.
63. W. Luo, X. Hu, Y. Sun and Y.Huang, *ACS Appl. Mater. Interf.*, 2013, **5**, 1997-2003.
64. A. Sumboja, C. Y. Foo, X. Wang and P. S. Lee, *Adv. Mater.*, 2013, **25**, 2809-2815.
65. Y. Cui, X. Zhao and R. Guo, *Electrochim. Acta*, 2010, **55**, 922-926.
66. Q.-C. Sun, X. Xu, S. N. Baker, A. D. Christianson and J. L. Musfeldt, *Chem. Mater.*, 2011, **23**, 2956-2960.

TOC